

Bayesian Unsupervised Machine Learning Approach to Segment Arctic Sea Ice from SMOS

Herbert Christoph¹, Camps Adriano¹, Wellmann Florian², and Vall-Llossera Mercedes¹

¹Universitat Politècnica de Catalunya (UPC)

²RWTH Aachen University

November 16, 2022

Abstract

Microwave radiometry at L-band is sensitive to sea ice thickness (SIT) up to 60 cm. Current methods to infer SIT depend on ice-physical properties and data provided by the ESA's Soil Moisture and Ocean Salinity (SMOS) mission. However, retrieval accuracy is limited due to seasonally and regionally variable surface conditions during the formation and melting of sea ice. In this work, Arctic sea ice is segmented using a Bayesian unsupervised learning algorithm aiming to recognize spatial patterns by harnessing multi-incidence angle brightness temperature observations. The approach considers both statistical characteristics and spatial correlations of the observations. The temporal stability and separability of classes are analyzed to distinguish ambiguous from well-determined regions. Model uncertainty is quantified from class membership probabilities using information entropy. The presented approach opens up a new scope to improve current SIT retrieval algorithms, and can be particularly beneficial to investigate merged satellite products.

Hosted file

animation_a1.gif available at <https://authorea.com/users/525020/articles/595607-bayesian-unsupervised-machine-learning-approach-to-segment-arctic-sea-ice-from-smos>

Bayesian Unsupervised Machine Learning Approach to Segment Arctic Sea Ice from SMOS

Christoph Herbert^{1,2}, Adriano Camps^{1,2}, Florian Wellmann³, and Mercedes Vall-llossera^{1,2}

¹CommSensLab, Universitat Politècnica de Catalunya (UPC) and Institut d'Estudis Espacials de Catalunya (IEEC/CTE-UPC), Barcelona, Spain

²Barcelona Expert Center (BEC), Barcelona, Spain

³Institute for Computational Geoscience and Reservoir Engineering, RWTH Aachen University, Aachen, Germany

Key Points:

- Retrieval algorithms to infer ice properties, such as sea ice thickness, exhibit high uncertainty due to limited knowledge of complexity
- An Unsupervised learning approach provides a synergistic framework which links data with the aim to recognize and analyze spatial patterns
- Bayesian segmentation of Arctic sea ice from SMOS data reveals stable and separable classes while indicating model uncertainty

Corresponding author: Christoph Herbert, herbert@tsc.upc.edu

Abstract

Microwave radiometry at L-band is sensitive to sea ice thickness (SIT) up to ~ 60 cm. Current methods to infer SIT depend on ice-physical properties and data provided by the ESA's Soil Moisture and Ocean Salinity (SMOS) mission. However, retrieval accuracy is limited due to seasonally and regionally variable surface conditions during the formation and melting of sea ice. In this work, Arctic sea ice is segmented using a Bayesian unsupervised learning algorithm aiming to recognize spatial patterns by harnessing multi-incidence angle brightness temperature observations. The approach considers both statistical characteristics and spatial correlations of the observations. The temporal stability and separability of classes are analyzed to distinguish ambiguous from well-determined regions. Model uncertainty is quantified from class membership probabilities using information entropy. The presented approach opens up a new scope to improve current SIT retrieval algorithms, and can be particularly beneficial to investigate merged satellite products.

Plain Language Summary

Remote sensing techniques are commonly used to provide maps of sea ice thickness (SIT). Methods to obtain these maps are based on the sea ice composition and on the signal measured by satellite. Sea ice Composition is spatially complex and changes during its formation and melting. Currently used data from observations of ESA's Soil Moisture and Ocean Salinity (SMOS) mission depend on several sea ice parameters, which hinders good estimation of almost any specific sea ice parameter. In this work, a new method to combine the information contained in SMOS brightness temperature data is investigated, with the aim to divide the Arctic region into a number of smaller areas – so called classes. Useful information about sea ice is contained in the spatial and statistical distribution of SMOS data, which are collected at different incidence angles. The relationship between the observations and the statistical properties of the obtained classes allow an assessment of its degree of separability and uncertainty. How classes change in time is used to estimate their temporal stability. The presented approach can be used to investigate the link between a variety of spatial datasets to improve current SIT products, and can be applied in many scientific fields.

1 Introduction

The Arctic region shows strong positive feedback to global warming and is very sensitive to climate change. Arctic sea ice has been declining, with the sea ice minimum for September 2020 ending up being the second lowest in the 42-year satellite record (NSIDC, 2020). Sea ice governs heat transfer and influences atmospheric circulation, which is particularly important because low- and mid-latitude's climates are closely related to polar climate (Overland & Wang, 2010; Francis & Vavrus, 2012). Monitoring of both sea ice concentration (SIC), as the fraction of sea-ice cover within an observed cell, and sea ice thickness (SIT) are necessary for a consistent determination of sea ice dynamics. Microwave radiometry is independent of daylight and at lower microwave frequency it is mostly unaffected by atmospheric conditions. The emissivity in the microwave spectrum depends on the dielectric properties of sea ice, which are a function of its physical composition including salinity, density, surface temperature, and surface roughness. In addition, the signal is emitted from a radiating layer which depends on the penetration depth of the sensor. Therefore, the separability of surface properties, such as open water and sea ice including SIT, is - in theory - feasible.

Several algorithms to retrieve SIT and SIC from brightness temperature (T_b) of satellite observations at Arctic scale have been developed, and various products have been deployed (Huntemann et al., 2014; Tian-Kunze et al., 2014; Kaleschke et al., 2016; Ricker et al., 2017; Gupta et al., 2019; Lavergne et al., 2019). ESA's Soil Moisture Ocean Salin-

ity (SMOS) mission (Font et al., 2009; Kerr et al., 2010) provides multi-incidence angle full-polarization T_b maps at L-band (1.4 GHz), which show sensitivity to thin sea ice. However, sea ice is under continuous transformation showing regional and seasonal variability. Physics-based methods to retrieve SIT strongly rely on knowledge of the ice-physical parameters. These parameters are estimated from empirically determined properties of different ice types (e.g. first- or multi-year ice). Thus, models can be subject to over-simplification, and model uncertainty is difficult to estimate, especially at Arctic scales considering an entire year. Validation capability is also limited due to sparsely available, only regionally and seasonally acquired, in-situ and airborne data. SIT retrieval algorithms perform well during Arctic freeze-up (Kaleschke et al., 2016), whereas heterogeneous conditions of sea ice during summer melt and limited spatial resolution of satellite observations make SIT estimation highly ambiguous. Therefore, SIT maps of sufficient quality are only available from mid-October to mid-April.

In this study, a data-based approach is investigated to segment Arctic sea ice, assuming that independent information about its properties are captured in the SMOS multi-incidence angle T_b dataset. The aim is to yield a framework to reveal spatial patterns from differences and similarities in the sensitivity of T_b observations to sea ice properties using an unsupervised learning algorithm. A Bayesian inferential model based on Gaussian Mixture Models (GMM) and Hidden Markov Random Fields (HMRF) considers both the statistical characteristics and the spatial correlations of the observations (Wang et al., 2017). The Arctic region is reduced to a relevant number of spatial classes, while keeping the probabilistic distribution for subsequent cluster analysis and uncertainty quantification. Spatial information is provided in terms of a latent field in physical space and statistical information is indicated by the means and covariances of the obtained classes in the feature space. A direct inference of sea ice properties, particularly at the ocean-ice-boundary, is ambiguous because SMOS observations can be sensitive to both SIC and thin sea ice. Therefore, T_b observation consisting of open water, and low SIC are corrected using SIC maps of the OSI-401-b product, provided by the European Organisation for the Exploitation of Meteorological Satellites (EUMETSAT). The polarization ratio (PR) between horizontally and vertically polarized values is selected for segmentation to increase the sensitivity to sea ice signatures by reducing the effect of physical surface temperature.

2 Data and Methods

In this study, PR maps at multi-incidence angles are obtained from SMOS T_b observations and OSI-401-b SIC maps, and are used to segment the Arctic ocean into sub-regions based on different sea ice properties. The proposed unsupervised machine learning approach is based on a Bayesian inference framework (Wang et al., 2017). The aim is to indicate patterns in a latent field in physical space according to the most relevant T_b observations. The temporal evolution of these patterns can be analyzed in terms of cluster separability and correlation of the input features to investigate the corresponding sea ice signatures.

2.1 SMOS multi-incidence angle T_b data

ESA's SMOS mission was originally designed to provide global and frequent maps of soil moisture and ocean salinity, but measurements also show sensitivity to different sea ice properties (thin SIT and SIC). The SMOS satellite is equipped with the Microwave Imaging Radiometer with Aperture Synthesis (MIRAS), an interferometric radiometer operating at L-band (~ 1.4 GHz) that acquires multi-incidence angle ($0-60^\circ$) full polarization T_b in ascending (6 a.m.) and descending (6 p.m.) sun-synchronous orbit (Corbella et al., 2005). T_b maps are retrieved with a radiometric resolution between 0.8-2.2 K, a spatial resolution of ~ 35 km at centre of field of view, and a revisit time of $\sim 1-3$ days

117 (Famiglietti et al., 2008). The retrograde polar orbit (98.42° inclination and 758 km al-
 118 titude) limits the observations to a maximum latitude of $\sim 84^\circ$, resulting in missing val-
 119 ues around the poles ('polar hole'). The input dataset for this study is given by the SMOS
 120 Level 1B data product consisting of the Fourier components of T_b in the antenna po-
 121 larisation reference frame. The high jump discontinuities in T_b between land and sea ob-
 122 servations lead to oscillations after image reconstruction at coastal areas (Gibbs phenomenon).
 123 These contaminated zones, as well as continental land mass, were removed in the data
 124 product. Ascending and descending SMOS observations show only small differences in
 125 T_b . Therefore, T_b of both orbits are averaged. A daily multi-angular dataset with 2°
 126 sampling is created similar to Gabarró et al. (2016) with T_b provided in horizontal and
 127 vertical polarization.

128 2.2 Input features selection

129 The study period includes the late summer melt and the first half of the freeze up
 130 period from September 1 to December 31, 2016. T_b data are averaged over 5 days to guar-
 131 antee full coverage of the Arctic ocean. Pixels of T_b images either consist of sea ice with
 132 ($0 < SIC \leq 1$), or purely consist of open water ($SIT = 0$). The sea ice surface repre-
 133 sents a grey body, and T_b is the product of the emissivity (ϵ) and the physical temper-
 134 ature (T_{Phys}), which is non-negligible in the lower microwave spectrum and varies de-
 135 pending on the atmospheric conditions among the Arctic. Therefore, input data for seg-
 136 mentation are selected with the objective to correct for SIC and to reduce the effect of
 137 spatial and temporal variability of T_{Phys} on T_b . In addition, direct inference of specific
 138 sea ice properties, particularly at the ocean-ice-boundary, is ambiguous by the fact that
 139 T_b can be sensitive to both SIC and thin SIT.

140 In a first step, $T_{b(SI)}$ was determined from the observed T_b , SIC, and the freezing
 141 point of seawater ($T_{b(OW)}$) (eq. 1).

$$142 \quad T_b = \alpha T_{b(SI)} + (1 - \alpha) T_{b(OW)} \quad \text{with} \quad \alpha \in [0, 1] \quad \text{and} \quad T_b = \epsilon T_{Phys} \quad (1)$$

143 Hereby, OSI-401-b SIC maps are provided in a polar stereographic projection grid at 10 km
 144 resolution and are regridded and upscaled to SMOS resolution using kd-tree resampling.
 145 $T_{b(OW)}$ are determined at different incidence angles and polarizations by evaluating the
 146 coldest values obtained for observations with low SIC located at latitudes above 75°N .
 147 SIC is often underestimated with respect to SIT, resulting in an overestimation of T_b ,
 148 which particularly influences the segmentation of areas covered by thin ice along sea ice
 149 edges. Therefore, a SIC threshold of $\alpha=0.5$ was chosen to provide an open water mask
 150 and to exclude observations classified with low SIC, which limits the overestimation er-
 151 ror.

152 In a second step, to account for variations in T_{Phys} , the polarization ratio (PR)
 153 is computed as the normalized difference between vertically and horizontally polarized
 154 values ($T_{b(SI,V)}$ and $T_{b(SI,H)}$) as follows

$$155 \quad PR = \frac{T_{b(SI,V)} - T_{b(SI,H)}}{T_{b(SI,V)} + T_{b(SI,H)}} = \frac{\epsilon(SI,V) - \epsilon(SI,H)}{\epsilon(SI,V) + \epsilon(SI,H)}, \quad (2)$$

156 which reduces to the emissivities of sea ice with the advantage of enhancing the sensi-
 157 tivity to the actual sea ice properties. $T_{b(SI,V)}$ is higher than $T_{b(SI,H)}$ with larger differ-
 158 ences for increasing incidence angles. Also, emissivity depends on the optical path length
 159 through sea ice, and PR increases for observations at higher incidence angles. PR's ob-
 160 tained for high incidence angles showed sufficient sensitivity range over ice-covered area
 161 with values reaching from 0 (thick ice, saturation) to ~ 0.3 (thin ice) and its distribu-
 162 tion depends on the observed period. Selecting PR values for high angles increases the
 163 content of independent information about sea ice, whereas values at lower angles are more
 164 likely to contain redundant information, which may lead segmentation biases. An assess-
 165 ment of the dominant features of SMOS data showed that sufficient angular variability

166 of SMOS T_b can be already obtained using three incidence angles. Therefore, PR maps
 167 at 40° , 48° and 56° are used as input features for segmentation.

168 2.3 Bayesian unsupervised machine learning algorithm

169 A Bayesian unsupervised machine learning approach Wang et al. (2017) is employed,
 170 previously applied to extract patterns of subsurface heterogeneity from geophysical multi-
 171 source data (Wang et al., 2019; Herbert et al., 2019). A Gaussian Mixture Model (GMM)
 172 is used to fit N data points (image pixels) in an M -dimensional space (M number of fea-
 173 tures) to find an optimal set of multivariate Gaussian distributions (L classes). The dis-
 174 tributions are parametrized by their means $\mu_{\theta,l}$ and covariances $\Sigma_{\theta,l}$ for each cluster l
 175 and incidence angle θ . Since features originate from satellite observations, a Hidden Markov
 176 Random Field (HMRF) is used to consider the statistical characteristics of data points
 177 in feature space as well as their spatial dependencies. A directional smoothing coefficient
 178 β accounts for anisotropy conditions with the assumption that neighboring pixels are more
 179 likely to belong to the same class. The segmentation results in a latent field x of hid-
 180 den variables, which indicates the most probable class membership as well as the prob-
 181 ability $p(x_i)_l$ of each pixel i to belong to class $l \in L$. The segmentation procedure is
 182 described in detail in Wang et al. (2017). The model parameters (μ, Σ, β) as well as the
 183 latent field x are obtained through Bayesian optimization in an iterative sampling pro-
 184 cess using a Markov Chain Monte Carlo (MCMC) approach after an initial Expectation-
 185 Maximization step. Prior to segmentation, the number of classes was predefined regard-
 186 ing the distribution of PR values. During late summer melt, only two significant classes
 187 are expected, comprising the remaining thick multi-year ice and regions of thinner ice.
 188 After sea ice minimum in mid-September, an additional third class is introduced, rep-
 189 resenting newly formed sea ice during freeze up. This choice is further approved by an
 190 a posteriori evaluation of cluster separability.

191 2.4 Cluster analysis

192 Results of the Bayesian segmentation are analyzed regarding the obtained patterns
 193 in physical space, and the location and orientation of clusters in feature space. The information-
 194 theoretic measure of entropy (H) is used to provide model uncertainty. It was initially
 195 defined by (Shannon, 1948) in the context of communication and has since been adapted
 196 to geosciences (Goodchild et al., 1994; Wellmann & Regenauer-Lieb, 2012). It is used
 197 to distinguish well-classified from uncertain regions and is defined by

$$198 \quad H(x_i) = - \sum_{l=1}^L p(x_i)_l \log(p(x_i)_l), \quad (3)$$

199 where $p(x_i)_l$ denotes the probability in the physical space of pixel i to belong to class
 200 l . H can reach values close to zero (pixel clearly assigned to one class) and $H_{max} = L[1 -$
 201 $\log(L)]$ (uniform distribution for L classes).

202 Sea ice properties, to which SMOS multi-incidence T_b are sensitive to, are dissim-
 203 ilar between classes and show similarities within the same class. Clusters in feature space
 204 are investigated regarding their location and orientation by analyzing the model param-
 205 eters μ and Σ . The correlation coefficient ρ quantifies the intra-cluster cohesion and can
 206 be used to distinguish between informative and redundant observations (Benesty et al.,
 207 2009). It is derived for each cluster from Σ in two-dimensional marginal space between
 208 features j and $k \in \{40^\circ, 48^\circ, 56^\circ\}$

$$209 \quad \Sigma_l = \begin{bmatrix} \Sigma_{jj} & \Sigma_{jk} \\ \Sigma_{kj} & \Sigma_{kk} \end{bmatrix}_l = \begin{bmatrix} \sigma_j^2 & \sigma_j \sigma_k \rho_{jk} \\ \sigma_k \sigma_j \rho_{kj} & \sigma_k^2 \end{bmatrix}_l, \quad (4)$$

210 where $\sigma_{j,k}$ correspond to the standard deviations with respect to feature j, k and $\rho_{jk} =$
 211 ρ_{kj} denote the correlation coefficients between two features, given by

$$212 \quad \rho_{jk} = \frac{\Sigma_{jk}}{\sigma_j \sigma_k} = \frac{\Sigma_{jk}}{\Sigma_{jj}^{1/2} \Sigma_{kk}^{1/2}}, \quad -1 \leq \rho_{jk} \leq 1. \quad (5)$$

213 The Geometric Separability Index (GSI) (Thornton, 1998) is a distance-based measure
 214 to analyze inter-cluster separability and is widely used for cluster interpretation (Greene,
 215 2001; Mthembu & Marwala, 2008). GSI compares all N data points with their nearest
 216 neighbor regarding their class membership and is defined by

$$217 \quad \text{GSI}(f) = \sum_{i=1}^N \frac{(f(x_i) + f(x'_i) + 1) \bmod 2}{N} \quad \text{with} \quad f(x_i) = \begin{cases} 1, & \text{if } x'_i = x_i \\ 0, & \text{if } x'_i \neq x_i \end{cases}, \quad (6)$$

218 where f is a binary target function, and x'_i is the nearest neighbor of x_i in the feature
 219 space of pixel i . $\text{GSI} \in [0.5, 1]$ and for values reaching its lower or upper limit, clusters
 220 are completely entangled or ideally separable, respectively. In this study, both global and
 221 cluster-specific separability are estimated. Global separability is computed based on Eu-
 222 clidean distance for all data points, and cluster-specific separability is obtained based
 223 on Mahalanobis distances $(x_i - \mu) \Sigma^{-1} (x_j - \mu)^T$, considering the data points and co-
 224 variances of the specific cluster (Mahalanobis, 1936). GSI is investigated along the study
 225 period to evaluate the dynamics of the underlying sea ice properties and the stability of
 226 the segmentation.

227 **3 Results**

228 Arctic sea ice is segmented independently for 5-day intervals into classes during the
 229 periods of late summer melt and early freeze up from September 1 to December 31, 2016.
 230 The latent field in physical space and the corresponding multivariate Gaussian distri-
 231 butions of data points in feature space are presented as an example for the segmenta-
 232 tion step interval between October 24-28, 2016 (sections 3.2 and 3.1). The temporal evo-
 233 lution of model parameters (cluster means and variation) is evaluated in section 3.3. Class
 234 membership and separability are assessed in section 3.4 to indicate cluster stability and
 235 performance of the algorithm.

236 **3.1 Latent field of classes in physical space**

237 The Figures 1a and 1b show the resulting latent field and the model uncertainty
 238 quantified by information entropy, respectively. The latent field indicates spatial patterns,
 239 which are acquired from the final iteration of the segmentation by assigning the class with
 240 highest probability to every pixel. Pixels with the probability to belong to two or more
 241 clusters have larger entropy and reflect therefore uncertain pixels. These pixels comprise
 242 regions at the boundary between classes and pixels, which are generally difficult to as-
 243 sign to any cluster. In the latter case, these pixels may point out sub-regions with dif-
 244 ferent sea ice properties (anomalies), which are characterized with high model uncertainty.

245 The segmented spatial patterns are compared to those of the SMOS L3 Sea Ice Thick-
 246 ness product, provided by the Alfred Wegener Institute (AWI) for Polar and Marine Re-
 247 search (Tian-Kunze et al., 2014). SIT means were computed according to the indicated
 248 spatial classes in each segmentation step, and averaged values are determined during freeze
 249 up from October 15 to December 31, 2016. The three classes can associated to differ-
 250 ent ice thickness (in meters) of 1.24 ± 0.10 , 0.54 ± 0.24 and 0.13 ± 0.07 , respectively. The
 251 classes are labeled as (0 $\hat{=}$ thick ice up to sensor saturation), (1 $\hat{=}$ transition zone with
 252 higher thickness variability, containing various ice types), and (2 $\hat{=}$ newly-formed thin
 253 ice).

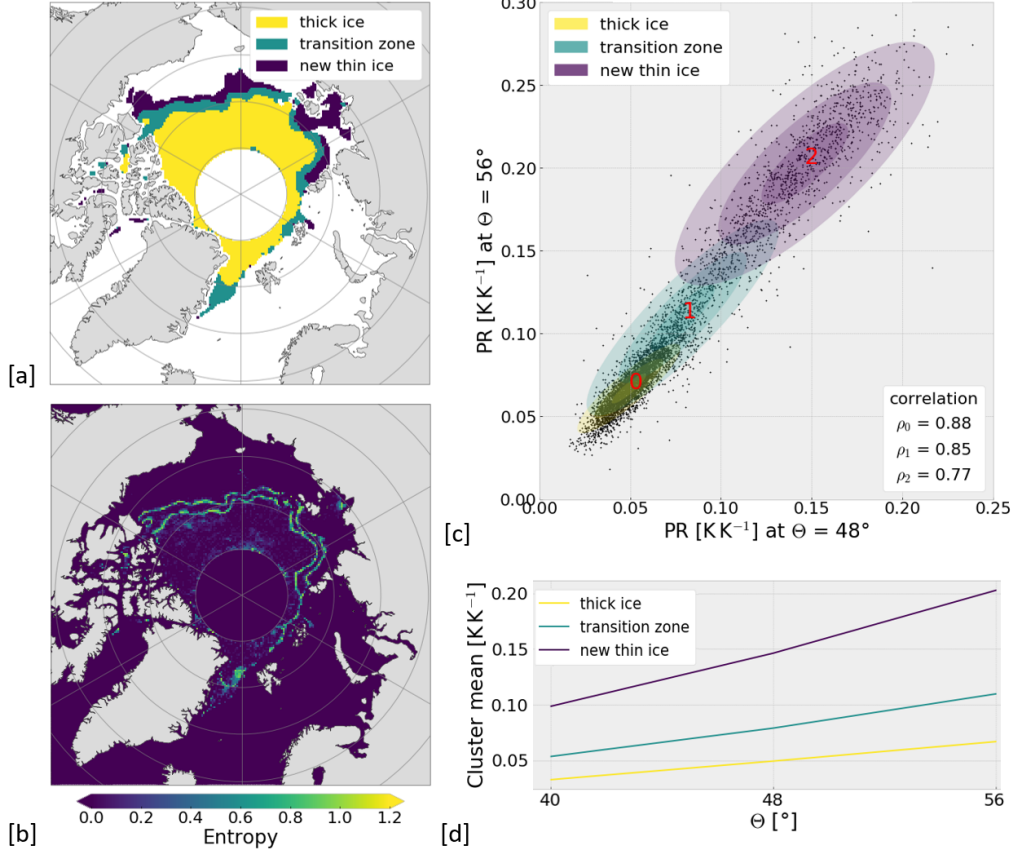


Figure 1. Segmentation result for observations between October 24 and October 28, 2016. [a] Latent field result for three classes. [b] Model uncertainty represented by information entropy based on label probabilities. [c] PR in marginal feature space between the incidence angles 48 and 56° and correlation for each cluster. [d] Variation of PR cluster means with incidence angle.

254

3.2 Clusters in feature space

255

256

257

258

259

260

261

262

263

264

265

266

267

268

269

Figure 1d illustrates the PR cluster means for different incidence angles. Higher values are obtained for higher incidence angles, characterized by different slopes within the same class, showing that the set of selected input features provides independent information about the sea ice surface. The multivariate Gaussian distributions with the corresponding clusters in marginal features space between the incidence angles 48 and 56° are illustrated in figure 1c. The correlation between the input features is generally higher for thick ice resulting in a well-determined cluster with higher intra-cluster cohesion. In contrast, newly-formed thinner ice shows less correlation between input features. This enables to discriminate classes of similar surface characteristics, to which multi-incidence angle observations show a different signature. However, sea ice is a complex medium and sea ice growth can occur under rougher or calmer ocean conditions, causing newly formed ice to be heterogeneous. These differences in the origin of sea ice formation might be captured in the input features, indicated by a broader distribution in marginal features space. On the contrary, the structures of multi-year thick ice appear more homogeneous.

270

3.3 Temporal evolution of clusters

271

272

273

274

275

276

277

278

279

280

281

282

283

284

285

286

287

288

289

Figure 2 shows the temporal evolution of cluster means and standard deviations (StDev) in marginal feature space for $\theta = 56^\circ$, and the distribution of PR and the corresponding class membership at three particular dates. The late summer melt comprises two significant classes until annual sea ice extent reaches its minimum (September 6, 2016). The evolution of cluster means is compared to the mean Arctic temperature, which is computed from daily 2 m temperature ERA5 reanalysis data for latitudes above 75°N and downloaded from the European Centre for Medium-Range Weather Forecasts (ECMWF) (C3S, 2017). Once Arctic temperatures drop long enough below the freezing point of saline sea water ($\sim -1.8^\circ\text{C}$) to allow sufficient heat transfer towards the atmosphere, new sea ice starts to form. Hence, a third class can be determined, which is represented by a significant number of PR values above 0.15. Cluster mean of thick ice is widely stable over the entire study period. Two phenomena can be observed regarding new thin ice. Firstly, its cluster mean decreases and gradually closes up with the transition zone. Secondly, an overlap between clusters can be observed in relation to strong positive temperature anomalies in the Arctic. This can be due to class imbalance arising from a decreasing amount of newly-formed ice, comparing to the total sea ice extent. Also, as the sea ice edge reaches lower latitudes during freeze up, which are characterized by different climate conditions, a decrease in PR values can be observed although a significant amount of sea ice is still being formed.

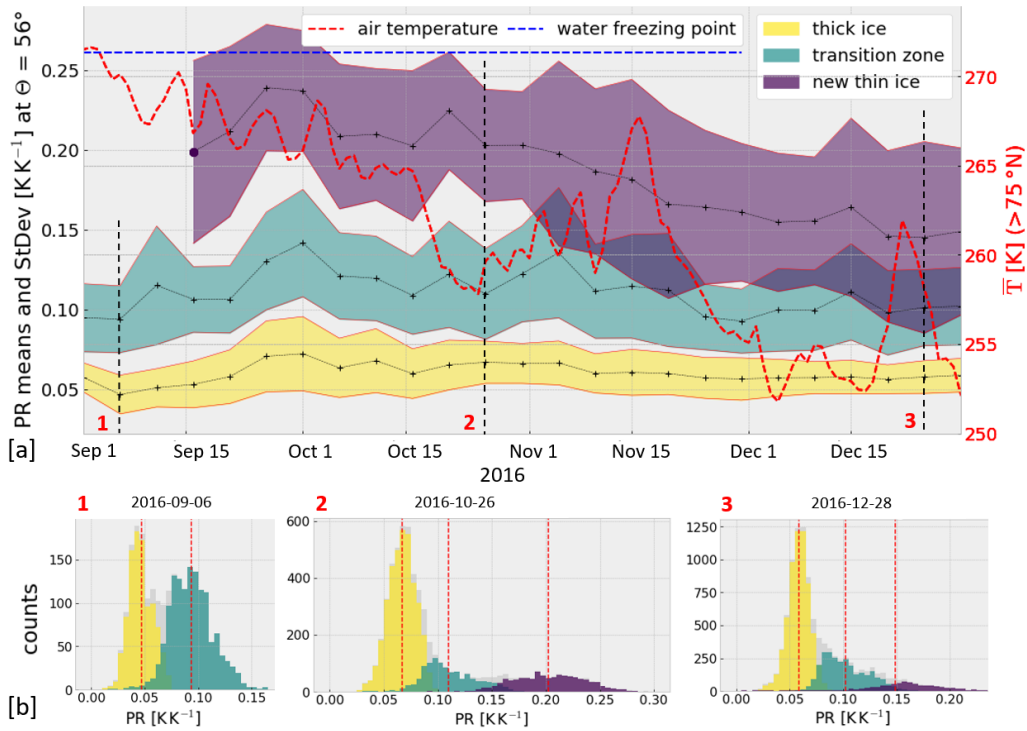


Figure 2. Temporal evolution of clusters. [a] Temporal evolution of cluster means and standard deviations at 56° incidence angle and mean Arctic temperature for latitudes $> 75^\circ\text{N}$. [b] PR distribution with respect to class membership at three particular dates (September 4-8, October 24-28 and December 24-28, 2016).

290

291

Figure 3a shows the evolution of the number of pixels per class membership for filtered sea ice ($\text{SIC} > 0.5$) in comparison to the total sea ice extent (SIE). SIE comprises

292 sea ice cover for $SIC > 0.15$ and daily data was downloaded from the data archive of the
 293 National Snow and Ice Data Center (NSIDC, 2020). Deviations and offsets between SIE
 294 and the total pixel counts are due to missing values within the ‘polar hole’ and contam-
 295 inated zones at the sea-land boundary. The increase of the total number of pixels is equiv-
 296 alent to a monthly growth rate in SIE of about $2.5 \times 10^6 \text{ km}^2$. The number of pixels con-
 297 sisting of newly-formed ice is broadly stable, whereas the number pixels classified as tran-
 298 sition zone are slightly increasing during freeze up. As sea ice grows, thick sea ice be-
 299 comes more abundant, leading to a log-normal-shaped PR distribution with increasing
 300 expected value (Figure 2b,3). Although thin ice becomes less representative in the data
 301 during freeze up, the algorithm is still capable of separating three classes as long as sea
 302 ice formation continues.

303 3.4 Separability of clusters

304 Global and cluster-specific separability are shown in figure 3b. The solid lines show
 305 the GSI for a choice of two classes in late summer melt and three classes during freeze
 306 up. High global separability is achieved along the entire study period with values around
 307 0.9. The cluster-specific GSI indicates separable classes with mean values of 0.95, 0.83
 308 and 0.83 for thick ice, transition zone and new sea ice, respectively. Along the freeze up,
 309 new thin ice starts to overlap with the transition zone and a threshold of minimum GSI
 310 needs to be defined to specify the appropriate number of classes for each segmentation
 311 step. For comparison, GSI is shown for the end of the summer melt period for a segmen-
 312 tation with three classes (dashed lines). In this case, classes highly overlap and the choice
 313 of two initial clusters from the beginning of the study period leads to higher separabil-
 314 ity.

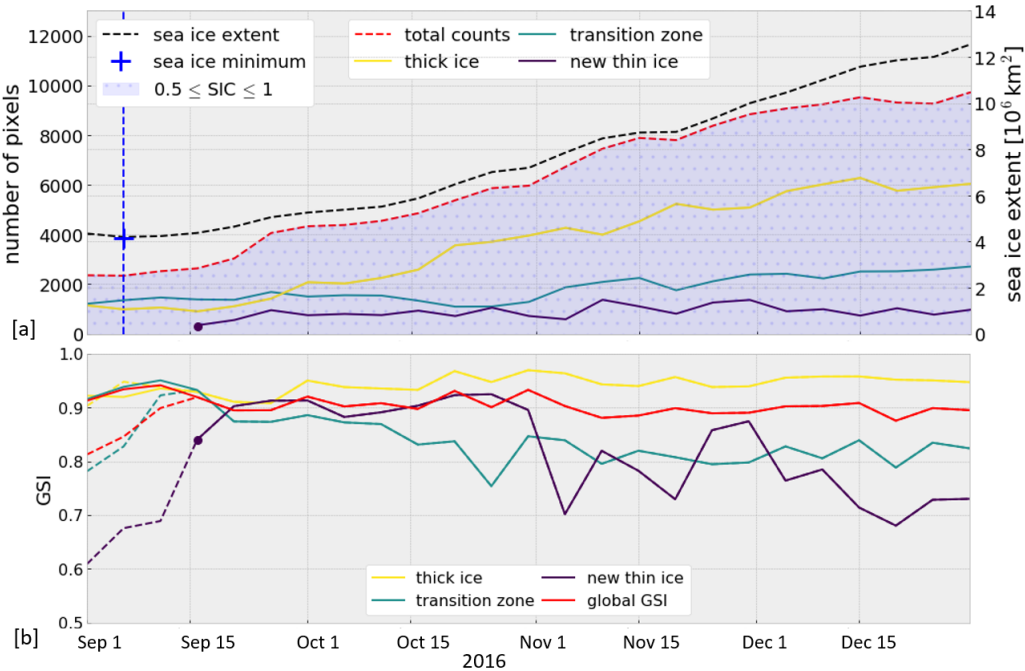


Figure 3. [a] Temporal evolution of class membership and sea ice extent, with indicated sea ice minimum and SIC. [b] Global and cluster-specific GSI along the observation period, determined from nearest-neighbor evaluation using Euclidean and Mahalanobis distances, respectively.

4 Discussion

A novel approach is evaluated to obtain sea ice maps from SMOS observations using Bayesian segmentation. The estimation of a constant number of stable and separable classes revealed periods, when T_b observations show similar sea ice signatures. The information content obtained by linking T_b data at multiple incidence angles and polarizations is reduced to a number of most significant classes, with good inter-cluster separability. The corresponding spatial patterns, which are indicated in the latent field result, can be used to extract the heterogeneity of the underlying sea ice properties.

Information entropy points out both uncertain zones between segmented classes and anomalies which can form sub-classes. As an example, ponded sea ice during summer melt has different surface characteristics, which may result in a further discriminable class only during that particular period. Since cluster means represent the most significant observations at every segmentation step, their temporal evolution can be used to define dynamic tie points. These tie points can be analyzed to investigate how sensitive input features respond to changes in sea ice signatures.

The implemented method serves as a framework to integrate multi-source datasets and is capable of recognizing patterns by considering the statistical characteristics and spatial correlations. The relationship of satellite observations at multiple frequencies can be used to select an appropriate set of input features and to enhance the sensitivity to ice-physical parameters, such as SIT. A combination of the presented data-driven segmentation approach with a physics-based inference model build upon the estimated distribution of classes may increase the retrieval accuracy of existing large-scale sea ice products.

5 Conclusion

In this work, Arctic sea ice is classified using a Bayesian unsupervised learning approach by making full use of the information about sea ice properties contained in the PR of SMOS multi-incidence angle T_b data. Sea ice properties are considered anisotropic as well as regionally and seasonally variable among the Arctic and T_b cannot be assumed to be sensitive to similar properties over an entire year. Therefore, both statistical characteristics of observations are evaluated and the segmentation is carried out by means of a discretized number of spatially regularized classes. The number of classes was determined a priori from the PR distribution and was verified a posteriori using GSI. Model uncertainty was determined using information entropy and enabled to distinguish well-determined from uncertain regions. High global separability was achieved considering two classes during late summer melt and three classes during freeze up, respectively. A comparison with existing SMOS-SIT maps indicated that classes can be attributed to SIT ranges. During late summer melt, two classes could be attributed to remaining thick ice and a transition zone, showing differences in the correlations of the input features. With the beginning of the formation of new thin ice during freeze up, an additional class could be discriminated based on the occurrence of higher PR values. However, the decrease in relative abundance of newly formed ice to the total sea ice during freeze up resulted thin sea ice to be less significant and led to higher overlap between classes. The underlying sea ice properties and the corresponding variation in PR have to be better understood to draw conclusions of the obtained classes, considering an entire annual cycle of Arctic sea ice formation and melting.

Acknowledgments

There are no perceived conflicts of interest for the lead author or coauthors. The lead author received the support of a fellowship from “la Caixa” Foundation (ID 100010434). The fellowship code is LCF/BQ/DI18/11660050. This project has received funding from

364 the European Union’s Horizon 2020 research and innovation programme under the Marie
 365 Sklodowska-Curie grant agreement No. 713673. It was also funded through the award
 366 ”Unidad de Excelencia María de Maeztu” MDM-2016-0600, by the Spanish Ministry of
 367 Science and Innovation through the project ”L-band” ESP2017-89463-C3-2-R, and the
 368 project ”Sensing with Pioneering Opportunistic Techniques (SPOT)” RTI2018-099008-
 369 B-C21/AEI/10.13039/501100011033. The authors would also like to thank Carolina Gabarro
 370 from the Barcelona Expert Center for providing the processed SMOS L1C data. The pro-
 371 duction of the SMOS-SIT data was funded by the ESA project SMOS & CryoSat-2 Sea
 372 Ice Data Product Processing and Dissemination Service, and data from October 15 to
 373 December 31, 2016 were obtained from AWI ([https://smos-diss.eo.esa.int/socat/
 374 L3_SIT_Open](https://smos-diss.eo.esa.int/socat/L3_SIT_Open)).

375 References

- 376 Benesty, J., Chen, J., Huang, Y., & Cohen, I. (2009). Pearson correlation coefficient.
 377 In *Noise reduction in speech processing* (pp. 1–4). Springer.
- 378 C3S. (2017). *ERA5: Fifth generation of ECMWF atmospheric reanalyses of the*
 379 *global climate*. <https://cds.climate.copernicus.eu/cdsapp#!/home>.
 380 Copernicus Climate Change Service Climate Data Store (CDS). (Accessed:
 381 2020-01-10)
- 382 Corbella, I., Torres, F., Camps, A., Colliander, A., Martín-Neira, M., Ribó, S., ...
 383 Vall-llossera, M. (2005). Miras end-to-end calibration: Application to smos
 384 l1 processor. *IEEE Transactions on Geoscience and Remote Sensing*, 43(5),
 385 1126–1134.
- 386 Famiglietti, J. S., Ryu, D., Berg, A. A., Rodell, M., & Jackson, T. J. (2008). Field
 387 observations of soil moisture variability across scales. *Water Resources Re-*
 388 *search*, 44(1).
- 389 Font, J., Camps, A., Borges, A., Martín-Neira, M., Boutin, J., Reul, N., ... Meck-
 390 lenburg, S. (2009). Smos: The challenging sea surface salinity measurement
 391 from space. *Proceedings of the IEEE*, 98(5), 649–665.
- 392 Francis, J. A., & Vavrus, S. J. (2012). Evidence linking arctic amplification to ex-
 393 treme weather in mid-latitudes. *Geophysical research letters*, 39(6).
- 394 Gabarró, C., Pla Resina, J., Turiel, A., Portabella, M., Martínez, J., Olmedo, E., &
 395 González, V. (2016). Arctic sea ice concentration estimation with smos data.
- 396 Goodchild, M., Chih-Chang, L., & Leung, Y. (1994). Visualizing fuzzy maps. *Visu-*
 397 *alization in geographical information systems*, 158–167.
- 398 Greene, J. (2001). Feature subset selection using thornnton’s separability index and
 399 its applicability to a number of sparse proximity-based classifiers. In *Pro-*
 400 *ceedings of annual symposium of the pattern recognition association of south*
 401 *africa*.
- 402 Gupta, M., Gabarro, C., Turiel, A., Portabella, M., & Martinez, J. (2019). On
 403 the retrieval of sea-ice thickness using smos polarization differences. *Journal of*
 404 *Glaciology*, 65(251), 481–493.
- 405 Herbert, C., Wellmann, F., Wang, H., & Hebel, C. v. (2019). Extracting hetero-
 406 geneity of subsoil from geophysical measurements using unsupervised learning
 407 algorithms. In *Geophysical research abstracts* (Vol. 21).
- 408 Huntemann, M., Heygster, G., Kaleschke, L., Krumpen, T., Mäkynen, M., & Dr-
 409 usch, M. (2014). Empirical sea ice thickness retrieval during the freeze up
 410 period from smos high incident angle observations. *The Cryosphere*, 8(2),
 411 439–451.
- 412 Kaleschke, L., Tian-Kunze, X., Maaß, N., Beitsch, A., Wernecke, A., Miernecki, M.,
 413 ... others (2016). Smos sea ice product: Operational application and valida-
 414 tion in the barents sea marginal ice zone. *Remote Sensing of Environment*,
 415 180, 264–273.
- 416 Kerr, Y. H., Waldteufel, P., Wigneron, J.-P., Delwart, S., Cabot, F., Boutin, J., ...

- 417 others (2010). The smos mission: New tool for monitoring key elements of the
418 global water cycle. *Proceedings of the IEEE*, *98*(5), 666–687.
- 419 Lavergne, T., Sørensen, A. M., Kern, S., Tonboe, R., Notz, D., Aaboe, S., ... oth-
420 ers (2019). Version 2 of the eumetsat osi saf and esa cci sea-ice concentration
421 climate data records. *Cryosphere*, *13*(1), 49–78.
- 422 Mahalanobis, P. C. (1936). On the generalized distance in statistics..
- 423 Mthembu, L., & Marwala, T. (2008). A note on the separability index. *arXiv*
424 *preprint arXiv:0812.1107*.
- 425 NSIDC. (2020). *Arctic sea ice at minimum extent for 2020 (September 2020)*.
426 [https://nsidc.org/news/newsroom/arctic-sea-ice-minimum-extent](https://nsidc.org/news/newsroom/arctic-sea-ice-minimum-extent-2020)
427 -2020. Boulder, Colorado USA. NASA National Snow and Ice Data Center.
428 (Accessed: 2020-10-08)
- 429 Overland, J. E., & Wang, M. (2010). Large-scale atmospheric circulation changes are
430 associated with the recent loss of arctic sea ice. *Tellus A*, *62*(1), 1–9.
- 431 Ricker, R., Hendricks, S., Kaleschke, L., Tian-Kunze, X., King, J., & Haas, C.
432 (2017). A weekly arctic sea-ice thickness data record from merged cryosat-
433 2 and smos satellite data. *The Cryosphere*, *11*, 1607-1623. [https://doi.org/](https://doi.org/10.5194/tc-11-1607-2017)
434 [10.5194/tc-11-1607-2017](https://doi.org/10.5194/tc-11-1607-2017).
- 435 Shannon, C. E. (1948). A mathematical theory of communication. *The Bell system*
436 *technical journal*, *27*(3), 379–423.
- 437 Thornton, C. (1998). Separability is a learner’s best friend. In *4th neural computa-*
438 *tion and psychology workshop, london, 9–11 april 1997* (pp. 40–46).
- 439 Tian-Kunze, X., Kaleschke, L., Maaß, N., Mäkynen, M., Serra, N., Drusch, M., &
440 Krumpfen, T. (2014). Smos-derived thin sea ice thickness: algorithm baseline,
441 product specifications and initial verification. *The Cryosphere*, *8*, 997–1018.
- 442 Wang, H., Wellmann, F., Zhang, T., Schaaf, A., Kanig, R. M., Verweij, E., ...
443 van der Kruk, J. (2019). Pattern extraction of topsoil and subsoil hetero-
444 geneity and soil-crop interaction using unsupervised bayesian machine learning:
445 An application to satellite-derived ndvi time series and electromagnetic induc-
446 tion measurements. *Journal of Geophysical Research: Biogeosciences*, *124*(6),
447 1524–1544.
- 448 Wang, H., Wellmann, J. F., Li, Z., Wang, X., & Liang, R. Y. (2017). A segmenta-
449 tion approach for stochastic geological modeling using hidden markov random
450 fields. *Mathematical Geosciences*, *49*(2), 145–177.
- 451 Wellmann, J. F., & Regenauer-Lieb, K. (2012). Uncertainties have a meaning: Infor-
452 mation entropy as a quality measure for 3-d geological models. *Tectonophysics*,
453 *526*, 207–216.

Supporting Information for ”Bayesian Unsupervised Machine Learning Approach to Segment Arctic Sea Ice from SMOS”

Christoph Herbert^{1,2}, Adriano Camps^{1,2}, Florian Wellmann³, and Mercedes

Vall-llossera^{1,2}

¹CommSensLab, Universitat Politècnica de Catalunya (UPC) and Institut d'Estudis Espacials de Catalunya (IEEC/CTE-UPC),

Barcelona, Spain

²Barcelona Expert Center (BEC), Barcelona, Spain

³Institute for Computational Geoscience and Reservoir Engineering, RWTH Aachen University, Aachen, Germany

Contents of this file

1. Figures F1 to F2
2. Table T1

Additional Supporting Information (Files uploaded separately)

1. Animation A1

Corresponding author: Christoph Herbert, Department of Signal Theory and Communications (TSC), Technical University of Catalonia, Building D3, Jordi Girona 1-3, 08034 Barcelona, Spain.
(herbert@tsc.upc.edu)

October 20, 2020, 12:45pm

Introduction

The choice of the appropriate number of classes is justified from the distribution of input features and the class separability. Figure F1 shows the marginal distribution of the polarization ratio (PR) at an incidence angle of 56° at 4 particular dates including the end of summer melt and the early freeze-up. PR distributions are shown for segmentation with 2 and 3 classes, respectively. During late summer melt until sea ice minimum (September 10, 2016), the choice of two classes was expected from the shape of the PR distribution. With the beginning of the freeze-up period, higher PR values become more frequent and an additional class is expected. Class separability is indicated by the Geometric Separability Index (GSI) and was obtained subsequent to segmentation. From the segmentation step at September 16, 2016 onwards, segmentation with a choice of 3 classes results in higher separability.

The classes were labeled according to the sea ice thickness estimates of the available SMOS-SIT product (Tian-Kunze et al., 2014). Figure F2 visualizes the latent field result in comparison to SMOS-SIT maps at the segmentation step intervals October 19-23, November 8-12, and December 23-27, 2016. Class 0 predominately contains consolidated thick ice beyond the sensitivity range of L-band $>\sim 0.6$ m (sensor saturation), class 1 refers to a transition zone of multiple thickness and types, and class 2 can be attributed to newly-formed thin ice.

Table T1 summarizes the obtained class mean values and standard deviations, averaged over the freeze-up period from October 15 to December 31, 2016. At each segmentation step interval, SIT mean values for each class are calculated according to the spatial pat-

terns of the latent field result. The obtained values at each segmentation step are then averaged over the freeze-up. The classes 0 and 2 show less variation and form stable clusters along the entire period, whereas class 1 contains higher variation. All three classes show sufficient separability along the entire period.

Caption Animation A1 Animation of the spatial patterns of the latent field result in physical space at each segmentation step interval from September 1 to December 31, 2016, including the distribution of the PR at 56° incidence angle.

References

- Tian-Kunze, X., Kaleschke, L., Maaß, N., Mäkynen, M., Serra, N., Drusch, M., & Krumpfen, T. (2014). Smos-derived thin sea ice thickness: algorithm baseline, product specifications and initial verification. *The Cryosphere*, 8, 997–1018.

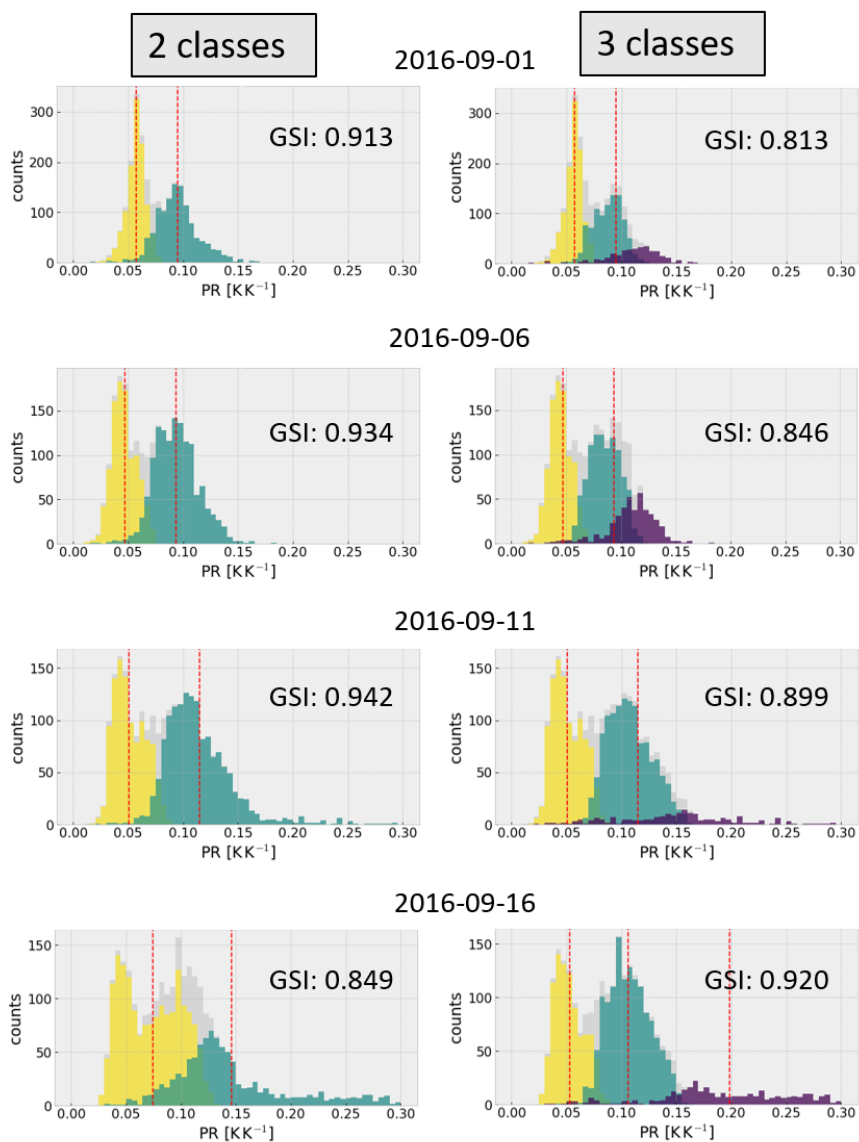


Figure F1. Distribution of PR values at 56° incidence angle for late summer melt and early freeze up from September 1 to September 16, 2016, including the indicated class membership and global separability (GSI), obtained for segmentation with 2 classes (left-hand side) and 3 classes (right-hand side), respectively.

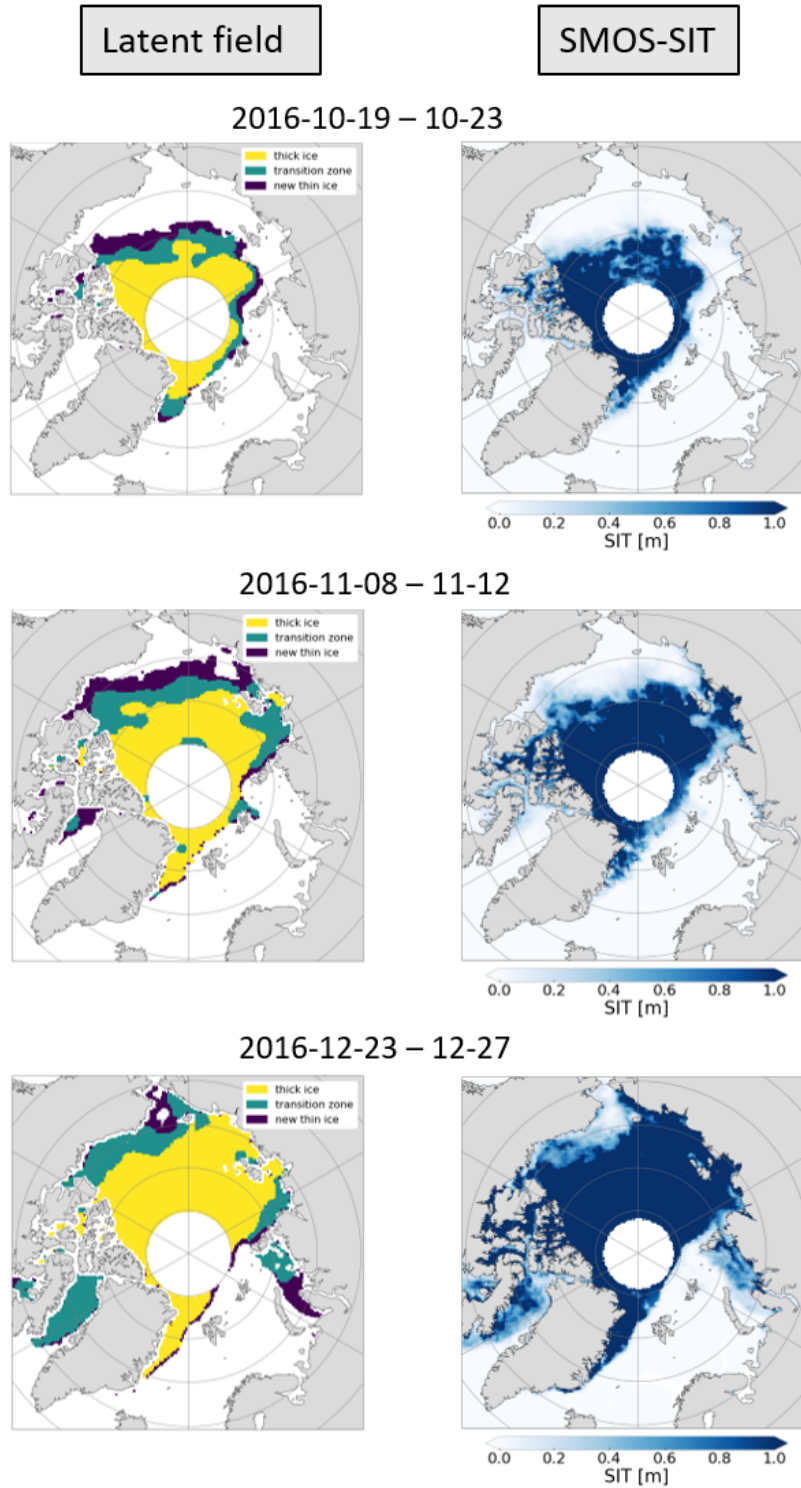


Figure F2. Comparison of the obtained latent field result with SIT maps of the SMOS-SIT product, averaged over the corresponding segmentation period (5-day interval).

Table T1. Summary of the temporal evolution of classes, evaluated within the freeze-up period from October 15 to December 31, 2016. Comparison of PR cluster mean values and standard deviations (StDev) at 56° incidence angle, including global separability (GSI), with the SMOS-SIT product.

Class	Label	PR mean	PR StDev	GSI	SMOS-SIT [m]
0	Thick ice	0.061 ± 0.005	0.014 ± 0.004	0.95 ± 0.02	1.24 ± 0.010
1	Transition zone	0.112 ± 0.012	0.028 ± 0.006	0.83 ± 0.04	0.54 ± 0.24
2	New thin ice	0.187 ± 0.03	0.048 ± 0.009	0.83 ± 0.08	0.13 ± 0.07